agriculture

MDPI

Article

Numerical Simulation and Optimization of Peanut Sheller Air–Screen Cleaning Device

Zhixia Liu [1,2], Yongqiang Yu [1], Jing Wang [1,2], Zhiwei Kang [1], Fengyu He [1,2,*] and Lianxing Gao [3,*]

[1] College of Engineering, Shenyang Agricultural University, Shenyang 110866, China; 1994500009@syau.edu.cn (Z.L.); yqyu98@126.com (Y.Y.); wj77@syau.edu.cn (J.W.); 2020240034@stu.syau.edu.cn (Z.K.)
[2] Key Laboratory of Horticultural Crop Agricultural Equipment, Ministry of Agriculture and Rural Affairs, Shenyang 110866, China
[3] College of Engineering and Technology, Jilin Agricultural University, Changchun 130118, China
* Correspondence: 1994500007@syau.edu.cn (F.H.); lianxing_gao@126.com (L.G.); Tel.: +86-13516039486 (F.H.); +86-13840375072 (L.G.)

Abstract: To improve its cleaning performance, the peanut sheller's air–screen cleaning device was used as the research object, and a numerical simulation was carried out. A scheme was proposed to optimize the installation angle of the screen surface of the air–screen cleaning device, and the influence of the airflow velocity of the sieve surface before and after the structural improvement of the machine on the airflow distribution of the whole chamber was evaluated. At the same time, the computational fluid dynamics–discrete element method (CFD–DEM) of coupling simulation was used to carry out single-factor simulation tests on the improved air–screen cleaning device, analyze the movement trajectory, velocity, and displacement of the extrudates in the cleaning chamber, characterize the separation law of extrudates, and determine the parameter ranges for each factor. In addition, based on the central composite Box–Behnken design, an orthogonal simulation test was carried out with three factors, including fan speed, amplitude, and vibration frequency, and the influence of each factor on the kernel loss rate and impurity rate was investigated. Furthermore, the influencing factors were optimized, and the optimal parameter combination was obtained; when the fan speed was 1682.72 r/min, the amplitude was 3.74 mm, and the vibration frequency was 492.86 Hz, it was more conducive to the cleaning of kernels. Finally, the accuracy of the simulation and optimization methods was verified via the machine test, and the optimal parameter combination was obtained: at a fan speed of 1680 r/min, an amplitude of 3.7 mm and a vibration frequency of 490 Hz were achieved, and the kernel loss rate and impurity rate were 2.01% and 2.42%, 3.71 and 4.42 percentage points lower than those before optimization, respectively.

Keywords: peanut sheller; air–screen cleaning device; numerical simulation; parameter optimization

check for updates

Citation: Liu, Z.; Yu, Y.; Wang, J.; Kang, Z.; He, F.; Gao, L. Numerical Simulation and Optimization of Peanut Sheller Air–Screen Cleaning Device. *Agriculture* **2023**, *13*, 1997. https://doi.org/10.3390/agriculture13101997

Received: 3 September 2023
Revised: 8 October 2023
Accepted: 13 October 2023
Published: 14 October 2023

Copyright: © 2023 by the authors. Licensee MDPI, Basel, Switzerland. This article is an open access article distributed under the terms and conditions of the Creative Commons Attribution (CC BY) license (https://creativecommons.org/licenses/by/4.0/).

1. Introduction

Peanut is a cash crop that blooms above ground and bears its fruit underground, and whether it is eaten raw, pressed into oil, or consumed as a seed, the soil on its surface or the air-entrained stones during harvesting has to be removed first, and then clean peanut kernels are obtained through hulling and cleaning [1–3]. Although the level of peanut harvesting and processing in China continues to improve, at present, the efficiency of kernels cleaning and the quality of kernels do not meet the existing industry standards. During the processes of peanut decladding, there are problems such as high cleaning loss and high impurity content [4–6], which seriously restrict the competitiveness in the peanut product market and the development of the food processing industry using peanut by-products [7–9].

The use of CAE technology to solve complex problems in agricultural machinery has become the primary technical means. Guo et al. conducted a discrete element method

(DEM) simulation of the working process of the bulldozing plate and compared the working resistance of the soil-engaging components with the results of the soil bin test; the microscopic process of soil disturbance was revealed from the perspective of simulation [10]. Shi et al. designed an active jet mixer and used the computational fluid dynamics (CFD) method to optimize the mixer structure [11]. Li et al. used an integrated approach of CFD–DEM to investigate the effects of using a cyclone spiral inlet on airflow patterns and bioparticle separation processes. The study's findings emphasized the critical role of inlet type and design in determining cyclone performance [12]. Zhi et al. used the CFD-DEM method; the jujube kinematic characteristics in the pneumatic pickup device's operation under positive and negative pressure airflow were studied, the pickup rate and loss rate of the equipment were used as response indicators, and the weight analysis method was used to calculate the forward speed and negative and positive pressure airflow velocity [13]. Hou et al. developed an air–screen castor cleaning device. Based on the discrete element method, the operating parameters of the cleaning device were optimized, and the parameters of the maximum screening efficiency combination, the minimum loss rate combination, and the best cleaning effect were obtained [14]. Chen et al. carried out an experiment using the CFD–DEM coupling method to carry out the numerical simulation of walnut shell–kernel cleaning, and the results showed that in the vertical air duct, the flow rate of the walnut shell would fluctuate around a fixed value, and the settlement rate of the walnut kernels would decrease with the increase in particle concentration and then gradually stabilize [15]. Mu et al. used the CFD–DEM coupling method to simulate the gas–solid flow in the throwing system of the sweet potato straw recycling machine, analyzed the internal airflow in the recycling machine, and obtained the movement law of the sorted materials [16]. Shi et al. used the CFD–DEM simulation technology to study the separation law of the exfoliated extrudates in the cleaning system of the flax combine harvester in hilly mountains and determined the optimal operating parameters based on the verification test [17]. The CFD–DEM coupling technology, used to simulate gas–solid flow, has become a reliable analysis method to study the motion law and parameter optimization of materials in agricultural cleaning machines. However, there is currently little research on numerical simulation for a cleaning device on the peanut sheller.

Combined with the physical characteristics of peanut extrudates and the theoretical analysis of the motion law in the process of cleaning materials, this paper used the CFD–DEM coupling method to numerically simulate the cleaning process of the HT–1000 peanut sheller so as to reveal the distribution of the airflow field velocity and the motion law of the peanut extrudates, and complete the optimization of structural parameters and operating parameters of the cleaning device, which can effectively reduce the kernel loss rate and impurity rate. We aim to provide theoretical reference and technical support for developing high-efficiency and low-loss cleaning equipment from a simulation perspective.

2. The Structure and Working Principle of the Peanut Sheller

2.1. The Complete Machine Structure

The machine is composed of a frame, feeding hopper, hulling device, concave plate screen, air–screen cleaning device, impurity removal fan, etc. (Figure 1). The impurity removal fan is located under the hulling drum, and the air–screen cleaning device is located under the impurity removal fan.

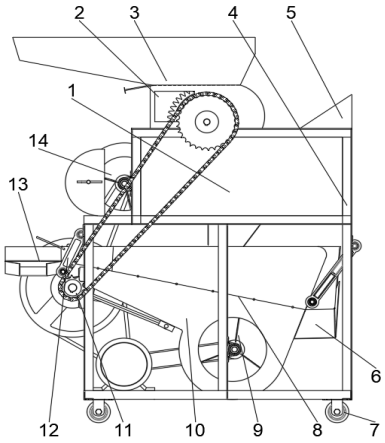


Figure 1. Schematic diagram of peanut sheller structure. 1. Air flow channel of the removing impurities fan. 2. Hulling device of peanut sheller. 3. The hopper of the peanut sheller. 4. Frame of peanut sheller. 5. Light impurity outlet. 6. Heavy impurity outlet. 7. Wheel. 8. Fish scale screen. 9. Air–screen cleaning device fan. 10. Air–screen cleaning device. 11. Eccentric. 12. Resonating arm. 13. Kernel outlet. 14. Fan for removing impurities.

2.2. Working Principle

The air–screen cleaning device consists of a fish scale screen, an eccentric wheel, a vibrating arm, and a fan (Figure 1). The peanut pods are dehulled through the interaction between the hulling drum and the concave plate sieve, and the extrudates formed fall on the fish scale sieve. Due to the difference in the size of each extrudates, the kernels with a higher specific gravity are in contact with the fish scale sieve under the action of airflow and vibration and are pushed through the sieve by the fish scale sieve. The pods with a low specific gravity intermittently in contact with the sieve surface under the action of airflow slide toward the tail of the sieve under the excitation of vibration to realize the separation of kernels and pods and complete the whole cleaning process.

2.3. The Preliminary Cleaning Test and Analysis of Influencing Factors

2.3.1. Test Conditions and Methods

The equipment used for hulling and kernel cleaning is the HT–1000 peanut sheller (Figure 2). The original operating parameters of the machine (Table 1) were tested, and with reference to the relevant Chinese standard test methods [18–21], the material used for the test was the blue and white 308 with the following parameters: the moisture content of pods was found to be between 8 and 12%, whereas the moisture content of kernels was between 9 and 14%, and the peanut feeding speed was 15–20 kg/min. Each test continued for three min, and the process of continuous and uniform feeding was completed by a specific person.



Figure 2. The peanut sheller.

Table 1. Main technical parameters of the peanut sheller.

Parameter	Numeric Value
Machine size (length × width × height), mm	1280 × 650 × 1300
Wind speed at the outlet of the removing impurities fan, m/s	12
fan speed, r/min	1900
Number of fan blades, pcs	3
Engine power, Kw	1.5
The size of the fish scale sieve (length × width), mm	800 × 240
The mounting angle of the fish scale sieve, °	10
The frequency of the vibrating screen, Hz	520
The amplitude of the vibrating screen, mm	3
The mounting angle of the vibrating arm, °	30

After the hulling and cleaning of each group, the kernel loss rate (Y_1) and the impurity rate (Y_2) were used as the evaluation indices and calculated using Equations (1) and (2); the measurements for each test were repeated three times and the average of the results were calculated. The test results are shown in Table 2.

$$Y_1 = \frac{W_3}{W_1 + W_2 + W_3} \times 100\% \quad (1)$$

$$Y_2 = \frac{W_2}{W_1 + W_2 + W_3} \times 100\% \quad (2)$$

where Y_1 is the kernel loss rate, %; Y_2 is the impurity rate, %; W_1 is the quality of the materials after the selection, g; W_2 is the quality of pods after selection, g; and W_3 is the quality loss of kernel, g.

Table 2. Results of the cleaning test.

Test Indicators	Loss Rate (%)	Miscellaneous Content (%)
The industry standard values	≤3	≤3
Test results	5.72	6.84
Test results after parameter adjustment	5.18	7.95

As seen in Table 2, the kernel loss rate and impurity rate were higher than the industry average standard values. There are many factors affecting the cleaning performance of the air–screen cleaning device, as one of the key components of the peanut sheller, during the cleaning process. In addition, during the test, the fan speed was adjusted to 1800 r/min, with an amplitude of 4 mm and a vibration frequency of 500 Hz, and the test was repeated. Compared with the original manufacturing parameters, the kernel loss rate and the impurity rate significantly changed.

Therefore, it is extremely important to carry out theoretical research and the optimization of relevant parameters to find the optimal parameters.

2.3.2. Force Analysis of Extrudates on the Screen Slope of Fish Scale

Screening on the fish scale sieve surface was carried out in a simple harmonic motion. The direction of the angular acceleration of the extrudates changed with the variation in the sieve surface acceleration, and the inertial force of the extrudates detachment was divided into four quadrants for analysis. Taking the inertial force of the extrudates as an example in quadrant three, the contact point O between the extrudates and the sieve surface is the coordinate of the origin, and the coordinate axes x-axis and y-axis were established in the opposite direction to the support force and friction force of the extrudates. The coordinate axis z was established perpendicular to the plane Oxy, and the force analysis was performed in the extrudates, as shown in Figure 3.

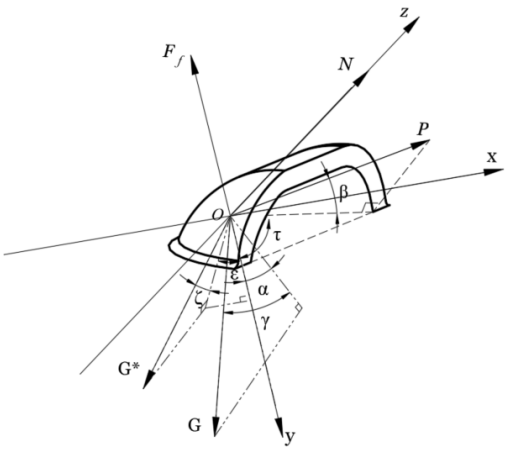


Figure 3. Force analysis of the extrudates at the slope of the sieve plate fish scale hole.

The force balance equation is as follows:

$$\begin{cases} N = Gsin\gamma + Gsin\zeta - Psin\beta \\ F_y = Pcos\beta\, cos\tau + G^*cos\zeta\, cos\varepsilon - \\ \quad F_f + Gcos\gamma\, cos\alpha \end{cases} \tag{3}$$

Therefore,

$$G = m \cdot g \tag{4}$$

$$G^* = m \cdot a_0 \tag{5}$$

$$P = C \cdot mv^2 \tag{6}$$

$$F_f = N \cdot tan\varphi \tag{7}$$

where N is the normal support force of the sieve surface, N; P is the airflow force exerted on the extrudates, N; G is the gravity of the extrudates, N; G^* is the inertial force exerted on the extrudates, N; a_0 is the acceleration of the exclamation point, m/s^2; F_f is the friction exerted on the extrudates, N; γ is the gravity projects the angle on the x–y plane, °; ζ is the inertial force projects the angle on the x–y plane, °; β is the airflow force projects the angle on the x–y plane, °; α is the gravity projects the angle on the y–z plane, °; τ is the airflow force projects the angle on the y–z plane, °; ε is the inertial force projects the angle on the y–z plane, °; v is the wind speed, m/s; C is the exfoliated float coefficient, m^{-1}; φ is the friction angle between the extrudates and the sieve surface, which is 25°.

The finishing Equations (3)–(7) are as follows:

$$\begin{cases} N = m\left(gsin\gamma + a_0 sin\zeta - Cv^2 sin\beta\right) \\ k = gsin\gamma + a_0 sin\zeta - Cv^2 sin\beta \\ F_y = mg(cos\gamma cos\alpha - sin\gamma) + ma_0(cos\zeta cos\varepsilon + sin\zeta tan\varphi) \\ + Cmv^2(cos\beta cos\tau - sin\beta tan\varphi) \end{cases} \tag{8}$$

where k is the ejection factor.

When $k < 0$, the extrudate is thrown off the sieve surface, and in the case of $k > 0$, the extrudate slides along the sieve surface. When $F_y > 0$, the extrudate slides backward along the sieve, and when $F_y < 0$, the extrudate slides forward along the sieve. During the screening process, the continuous change in air velocity and sieve surface acceleration caused the positive and negative changes in k; therefore, when the sieve surface acceleration occurs in the third quadrant, the extrudates have two states: thrown off or slipped through the fish scale sieve. Due to the special shape of the upper part of the sieve hole, the extrudate slides or is thrown at different angles with different positions on the fish scale sieve, indicating that the shape of the fish scale sieve would cause the extrudate to diverge around it.

2.3.3. Force Analysis of Extrudates on the Screen Plane of Fish Scale

The extruded material is mainly affected by the action of the airflow upon its contact with the fish scale sieve surface when it enters the air–screen cleaning device. The fan is set under the fish scale sieve, and the airflow is produced by the fan and then discharged through the screen hole, described as applying the fluid force based on the vibration of the extrudates so that the extrudates' process can generate movements at different speeds according to the force applied and separate, different trajectories.

There are three main states of the extrudates on the sieve surface: motionless, forward and backward movement, and starting and throwing. Due to the different acceleration directions of the sieve surface, this paper took the acceleration of the sieve surface as an example to analyze the force of the extrudates. The contact position between the extrudates and the sieve surface is the coordinate origin O, while the horizontal direction along the sieve surface is the coordinate x-axis, and the vertical direction along the sieve surface is the coordinate y-axis, as shown in Figure 4.

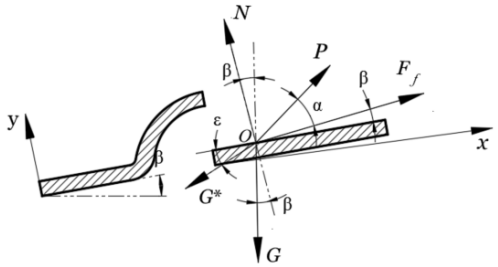


Figure 4. Force analysis of extrudates at the plane of the sieve plate fish scale holes.

Based on the force balance of the extrudates, Formula (9) is obtained as follows:

$$\begin{cases} N = Gcos\beta - Psin(\alpha - \beta) - G^*sin(\varepsilon - \beta) \\ F = F_f + Pcos(\alpha - \beta) - G^*cos(\varepsilon - \beta) - Gsin\beta \\ F_f = \begin{cases} Ntan\varphi(N \geq 0) \\ 0(N < 0) \end{cases} \\ G^* = -m\omega^2 Asin(\omega t) \end{cases} \tag{9}$$

where α is the angle between airflow and the sieve surface, °; ε is the vibration direction angle of the sieve, 25°; A is the amplitude, mm; β is the installation angle of the screen surface, 10°; F is the resultant force received by the peanut extrudates, N; ω is the angular velocity of the crank, rad/s; and t is the time, s.

The finishing Equation (9) is as follows:

$$\begin{cases} N = m\big(gcos\beta - Cv^2 sin(\alpha - \beta) - A\omega^2 sin(\omega t)sin(\varepsilon - \beta)\big) \\ F = mg(tan\varphi cos\beta - sin\beta) + Cmv^2 \\ \quad (cos(\alpha - \beta) - tan\varphi sin(\alpha - \beta)) - mA\omega^2 sin(\omega t) \\ \quad (tan\varphi sin(\varepsilon - \beta) - cos(\varepsilon - \beta)) \end{cases} \tag{10}$$

When $N \leq 0$, the extrudates are thrown up by the sieve surface. When $N > 0$, however, the extrudate slides along the plane of the sieve hole, wherein the $F > 0$ indicates the slide of the extrudate along the back side of the sieve, while the $F < 0$ indicates the slide along the front side of the sieve, and the extrudate remains stationary in relation to the sieve surface when $F = 0$.

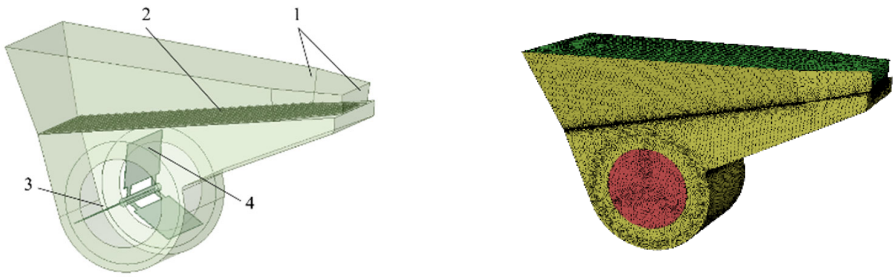
Based on the above analysis, the main factors affecting the cleaning performance of the air–screen cleaning device are fan speed, amplitude, and the angular velocity of the crank (vibration frequency). If the fan speed is too high or too low, the breakage of pods by the kernels or the removal of kernels by breaking open the pods occur. Too low an amplitude would cause difficulty in the stratification of the pods and kernels during the conveying process, making the separation of the pods and kernels difficult. On the other hand, the

extrudates jumps too much on the sieve surface or even jump off the sieve surface, resulting in kernel losses. If a certain range of the vibration frequency is not selected, cleaning and removing the pods and kernels during the conveying process would be carried out too quickly, and the screening effect would be poor.

3. The Simulation and Optimization of the Airflow Field

3.1. The CFD Model Establishment

Based on pilots and prototypes, to reduce the simulation calculation load and ensure the authenticity and reliability of the simulation model, the CFD model for the air–screen cleaning device was established, and the simplified three-dimensional model was created via the reverse drawing method in SOLIDWORKS. The size of the model was 900 mm × 400 mm × 600 mm, the angle between the fish scale sieve and the horizontal plane was 10°, the screen hole size was 17 mm × 5 mm × 5 mm, and the screen opening rate was 75%. The CFD model was imported into FLUENT Meshing, and the meshing process of the geometric model was performed using a wedge (*Poly*) mesh [22], which was optimized to achieve a distortion degree of less than 0.3. Subsequently, a total of 2,272,239 meshes were generated with an average high quality (Figure 5).



(**a**) (**b**)

Figure 5. The establishment of the CFD model and meshing. (**a**) The fluid domain model. 1. air-outlet 2. Fish scale screen 3. air-inlet 4. fan blades (**b**) The meshing of the flow field.

3.2. Parameter Settings

The mesh file was imported into the FLUENT system to set up the fluid simulation parameters, and the wall of the cleaning chamber was selected as a smooth wall according to the working environment of the cleaning chamber. The fluid was a non-compressible Newtonian fluid, while factors such as temperature and viscosity were ignored [23]. The air inlet in the air–screen cleaning device was set to pressure inlet, while the air outlet was fixed on pressure outlet; the interface blade of the rotation area was set to the dynamic grid, with the blade speed of 1700 r/min and the rotating flow surface of the rotation area. Moreover, the gravity direction taken was –Z direction with an acceleration of 9.81 m/s^2, and the realizable *k*–epsilon model was selected for the CFD simulation of the airflow. The numerical solution adopted the SIMPLEC algorithm, and the fluid medium was air, with a viscosity of 1.8×10^{-5} Pa·s and the residual accuracy set to 10^{-3}.

This research selects 44 cores, 88 threads, and 128 G running memory workstations as simulation tools. To reduce the error, firstly, the steady-state calculation is carried out for a period of time, and then the calculated result is used as the initial value of the transient analysis. The time step size is set to 0.001 s, the number of time steps is 5000, the Max Iterations/Time Step is 25, and the total time is 5 s.

3.3. Airflow Field Analysis

The air velocity and structure of the air–screen cleaning device directly affect the efficiency of the extrudates' cleaning. For the ease of conducting research, the Tecplot CFD 2020 R1 post-processing software was established to plot the x–z planes parallel to the y-axis at distances of 0 and 30 mm of the air–screen cleaning device, respectively, and the velocity contour contrast cloud diagram of the *t* time on these two planes could be obtained.

As seen in Figure 6, the gas flow rate along the x-axis (opposite to the outlet) shows the characteristics of the overall non-uniform attenuation on the x-axis on both measuring surfaces, and the time domain distribution of the overall flow rate varied greatly. On the 30 mm measuring surface, the x-axis of the 600–800 mm section created a "high–speed area", and the airflow velocity was high, showing a decreasing trend within the range of 8.21–9.56 m/s. The "high–speed area" along the x-axis of the 370–600 mm section above the screen surface decreased, the airflow velocity ranged from 4.4 to 6.32 m/s, and the upper part of the sieve surface was along the x-axis of the 0–350 mm section. The airflow velocity showed the phenomenon of the rise (high) in the middle and the fall (low) on the sides. Furthermore, the distribution of the airflow field showed an "M" shape curve, and the airflow velocity fell to a minimum of 2.01 m/s because the installation angle of the sieve surface was narrow and the direction of airflow through the holes of the sieve was parallel to the sieve surface. Therefore, the airflow was reduced when measuring the airflow parallel to the sieve. On the measuring surface of 60 mm, the "high–speed area" decreased further, but the "M" shaped area increased, as the influence of the mounting angle of the screen surface on the airflow velocity manifests with the increase in distance.

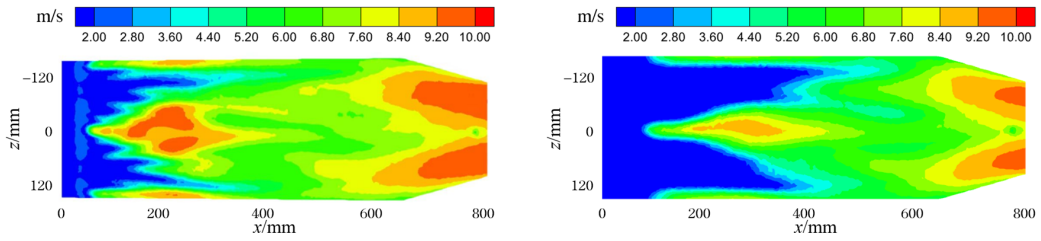


Figure 6. The cloud diagram of airflow velocity over each measuring surface of a sieve with an inclination angle of 10°. (**a**) The y-axis direction measures the surface airflow velocity at 30 mm. (**b**) The y-axis direction measures the surface airflow velocity at 60 mm.

Combined with the airflow velocity over each position inside the cleaning chamber, the sections 30 mm and 60 mm above the screen surface showed an uneven distribution of airflow, and the airflow attenuation at the back side of the sieve surface was faster. Moreover, considering the airflow velocity and distribution uniformity, the airflow field in the cleaning chamber should be optimized.

3.4. Optimization of the Airflow Field

3.4.1. Optimization of Goals

During the operation of the air–screen cleaning device, the basic conditions of air velocity need to be met. The airflow velocity above the sieve surface of the fish scale should be between that of the cleared material and the floating velocity of the debris, and at the same time, the air velocity should be less than the floating velocity of the pods [24,25]. However, if the air velocity through the sieve hole is greater than the floating speed of the pods, efficient screening cannot be achieved, and the kernel loss rate increases. If the wind velocity at the sieve hole is less than the kernels floating velocity, the impurity content of the kernel would increase, and the efficiency of cleaning (quality of the cleaned material) would decrease.

The airflow velocity and distribution of different measuring surfaces above the sieve surface can be intuitively seen using CFD simulation. Combined with the force analysis of the extrusion on the sieve surface described above, this research explores the airflow velocity and law of each measuring surface under different conditions of fish scale sieve angles (10°, 12°, and 14°) to improve the airflow field in the cleaning chamber.

3.4.2. Optimization of Results Analysis

Comparing the results of the simulation analysis at different installation angles of the sieve surface, it can be seen that when this angle was 12°, the overall airflow distribution of the measuring surface of 30 mm above the sieve was relatively uniform. Above the sieve surface along the x-axis of the section of 0–180 mm, the airflow created a "low–speed area", with a velocity of 2.02–3.61 m/s, and on the upper screen surface along the x-axis of the section of 210–530 mm, the airflow velocity was relatively uniform, fluctuating within the range of 4.45–7.57 m/s, conducive to the orderly stratification of extrudates. Observing the 60 mm measuring surface above the sieve, the "low–speed area" in the 0–160 mm section was smaller than the airflow field at the other two angles (10° and 14°), and the airflow velocity ranged between 2.29 and 2.98 m/s. In addition, the movement of pods in this area was not easily affected, conducive to the production of impurities during discharge. In the 190–660 mm section along the x-axis above the sieve surface, the fluctuation in airflow distribution along the z-axis and x-axis was small, ranging between 4.65 and 6.52 m/s, indicating a relatively stable distribution. At the same time, the air velocity at the kernels' outlet was relatively low, conducive to the stable discharge of the kernels (Figure 7). When the installation angle of the sieve surface was 14°, the gas flow on the measuring surface of the 30 mm sieve was along the x-axis (opposite the outlet), showing an uneven pattern of increasing first and then decreasing. Moreover, the air velocity along the x-axis of the 600–800 mm section above the sieve surface increased significantly to create a "high–speed area", which increased significantly compared with that with the installation angle of 10° (7.74–9.36 m/s). The air velocity fluctuated greatly along the x-axis of the 120–400 mm section above the screen surface, and the fluctuation ranged between 4.21 and 8.29 m/s. At the 60 mm measuring surface above the sieve, the "high–speed area" along the x-axis of the 600–800 mm section above the sieve surface was created at the exit mouth, with a maximum speed of 9.76 m/s. When the airflow velocity in the 200–400 mm section was higher than that of the area with the angle of 10°, the airflow distribution was still slightly uneven, and the high-speed area was created above the fan blades. The air velocity in the section of 0–200 mm increased compared with that of the area with the angle of 10°, which was between 2.76 and 7.99 m/s (Figure 8). Similarly, when the angle of the screen surface was 10° (original angle), the air velocity at the sections of 30 mm and 60 mm above the sieve surface was as described in Section 3.3.

In addition, the cloud diagram and flow line of the speed in the cleaning chamber on the x–y plane as the center plane of the air–screen cleaning device over the axial z = 0 point shows that the overall direction of the airflow within the cleaning chamber caused its entrance through the rotation of the fan blades so that it could act on the extrudates through the screen hole further to promote the forward movement of the extruded material (Figure 9). To summarize the simulation results, when the inclination angle of the sieve surface was 12°, the measured cross-section could generate a more ideal flow field.

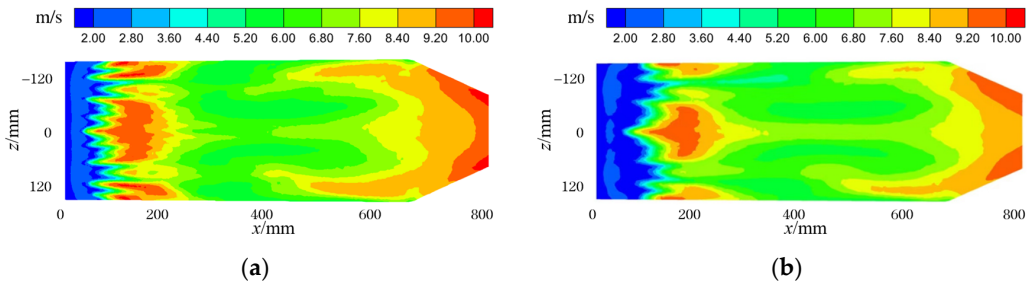
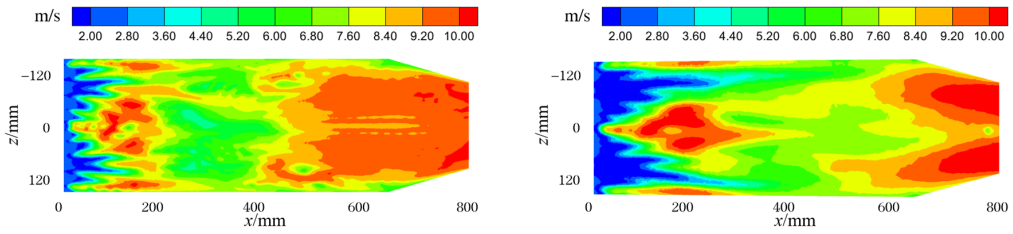
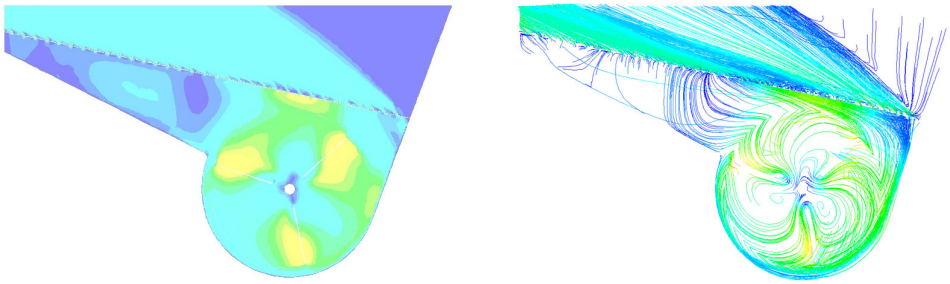


Figure 7. The cloud diagram of airflow velocity over each measuring surface of a sieve with an inclination angle of 12°. (**a**) The y-axis direction measures the surface airflow velocity at 30 mm. (**b**) The y-axis direction measures the surface airflow velocity at 60 mm.



(**a**) (**b**)

Figure 8. The cloud diagram of airflow velocity over each measuring surface of a sieve with an inclination angle of 14°. (**a**) The y-axis direction measures the surface airflow velocity at 30 mm. (**b**) The y-axis direction measures the surface airflow velocity at 60 mm.



(**a**) (**b**)

Figure 9. The speed cloud diagram and flow field trace diagram of air–screen cleaning device. (**a**) The speed cloud diagram. (**b**) The flow field trace diagram.

4. Simulation of Gas–Solid Two-Phase Flow

4.1. The DEM Model Establishment

According to the composition of the components present in the extrudates entering the air–screen cleaning device under actual working conditions, the discrete element method (DEM) simulation involved the unhulled pods (probabilistic approach due to the presence of shelled parts in the hulling process), intact kernels, half kernels, dust particles, and other small components. Each material has a different form, and dust particles and other fine residual components are usually ignored in the simulation analysis. After preliminary testing, the mass of the intact kernels accounted for 64.15% of the total mass of the extrudates, whereas the mass of the half kernels accounted for 20.94% of the total mass, and the unhulled pods accounted for 14.91% of the total mass of the extrudates in the air–screen cleaning device.

The particles were a combination of rigid body pellets of different sizes, and the three-dimensional particle (whole kernels) model (16.37 mm × 12.34 mm × 12.47 mm) was obtained via particle accumulation using the EDEM 2021.2 simulation software. The dimensions of the half kernels model are 16.25 mm × 5.22 mm × 12.05 mm, and the pods model has the dimensions of 32.86 mm × 15.67 mm × 16.49 mm (Figure 10).



(**a**) (**b**) (**c**)

Figure 10. The extrudates DEM model. (**a**) Whole kernels. (**b**) Half kernels. (**c**) Pods.

At the same time, new metal materials were built, and the materials' properties were set, i.e., the dynamic friction and static friction factors between the extrudates in the cleaning process were set, as shown in Table 3. Moreover, the contact parameters of the particle–particle and the particle–geometry are shown in Table 4, and Table 5 shows other parameters [26,27].

Table 3. The static/dynamic friction coefficients between the materials used in the DEM model.

Project	Pod	Whole Kernel	Half Kernel
Pod	0.40/0.60		
Whole kernel	0.06/0.18	0.06/0.42	
Half kernel	0.06/0.35	0.06/0.32	0.07/0.40
Model	0.10/0.40	0.03/0.20	0.06/0.30

Table 4. Recovery factors for the items used in the DEM model.

Project	Pod	Whole Kernel	Half Kernel
Pod	0.26		
Whole kernel	0.20	0.20	
Half kernel	0.30	0.20	0.50
Model	0.25	0.30	0.25

Table 5. The material attribute parameters used in the DEM model.

Project	Pod	Whole Kernel	Half Kernel	Model
Poisson's ratio	0.4	0.32	0.32	0.3
Shear modulus	6.5×10^6	5.06×10^7	5.06×10^7	7.99×10^7
Density/kg·m^{-3}	420	1030	1030	7800

The new pellet factory was dynamically generated upon the feeding inlet, with a virtual rectangular plane of 290 mm × 120 mm. The production rate of the whole kernels, half kernels, and pods was converted according to the actual operation process, and the total particle production time was set to 1 s. Since the extrudates are irregular in shape and have different sizes, there is a certain size of gap between the same grade of extrudates to be closer to the actual size. The initial model adopted a custom method for setting the volume, and its size fluctuated between 0.8 and 1.2 times the size of the extrudates' model; the initial speed at which the particles were added along the y-axis of each device was 0.5 m/s.

4.2. Parameter Settings

The parameters for fluid simulation using the FLUENT 19.2 software were set as per Section 3.1. The particle-to-particle contact model in EDEM used the Hertz–Mindlin (no slip) contact model. Similarly, the particle-to-geometry contact model also used the Hertz–Mindlin (no slip) contact model [28,29].

The FLUENT–EDEM coupling simulation needs to exchange bidirectional data, and set the time step for the simulation of these two to 1:100 times. After the simulation parameters of FLUENT and EDEM are set, the steady-state calculation is performed for a period of time to reduce errors, and then the EDEM coupling interface is opened, the load of the User Defined Function (UDF) coupling interface file in FLUENT (the coupling interface is dense discrete phase model (DDPM)), and the simulation calculation is completed after connection [30,31].

4.3. The Single-Factor Simulation Test

This section reveals whether the main factors that affect the kernel loss rate and the impurity rate are significant. The factors affecting the cleaning performance of the air–screen cleaning device mainly include fan speed, amplitude, and vibration frequency. The block statistical area (Figure 11) was established in the EDEM's post-processing tool module Selections to complete the statistical analysis of the kernel loss rate and the impurity rate.

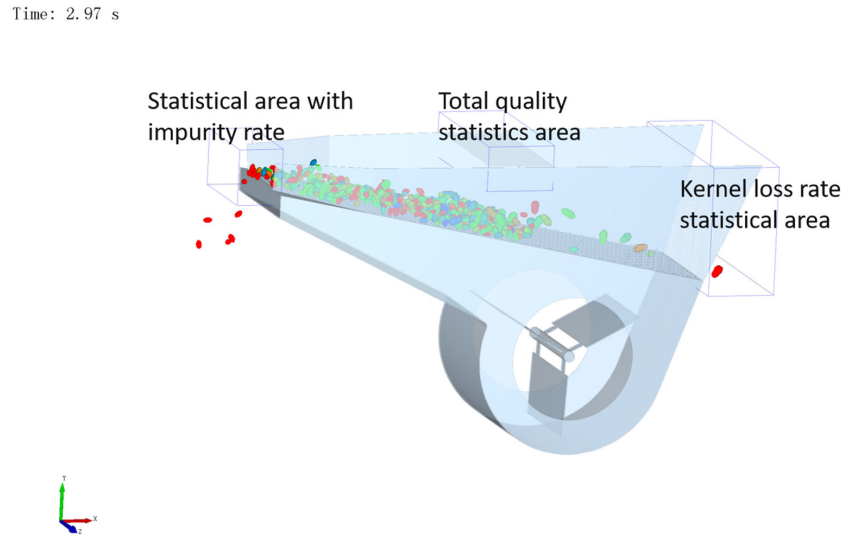


Figure 11. Statistical local area.

4.3.1. Effect of the Fan Speed on the Cleaning Performance

The amplitude and vibration frequency were set to 4 mm and 480 Hz, respectively, while the fan speed was set to five different levels of 1500 r/min, 1600 r/min, 1700 r/min, 1800 r/min, and 1900 r/min for the coupling simulation, and the kernel loss rate and impurity rate were statistically calculated after the simulation.

As shown in Figure 12, the fan speed was within the range of 1500–1600 r/min, and both the kernel loss rate and impurity rate first decreased and then increased. The reason is that the higher the speed, the greater the air velocity through the sieve hole, causing the rise in wind speed at the outlet of the kernels, resulting in the removal of pods by the kernels. Similarly, the lower the speed, the more difficult to effectively separate the kernels and the pods, resulting in the removal of the kernels by the pods. At the same time, the airflow generated by the fan had a greater rate than that from the extrudate with a high specific gravity or a lower rate than that from the extrudate with a low specific gravity, which caused poor layering, resulting in an excessively high impurity rate.

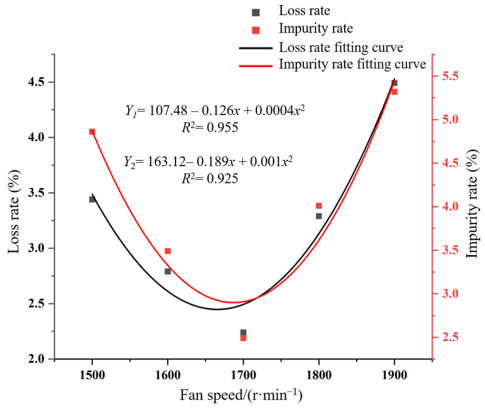


Figure 12. Effect of the fan speed on the cleaning performance.

4.3.2. Effect of Amplitude on the Cleaning Performance

This section focuses on five different levels of amplitude, including 2.0 mm, 3.0 mm, 4.0 mm, 5.0 mm, and 6.0 mm in the air–screen cleaning device, and sets the fan speed to 1700 r/min and the vibration frequency to 480 mm, followed by the calculation of the kernel loss rate and impurity rate after the simulation.

As shown in Figure 13, when the amplitude was within the range of 2–6 mm, the kernel loss rate increased with the increase in amplitude, because the larger the amplitude, the easier it is to make the kernels jump off the sieve surface, resulting in kernel loss. At the same time, with the increase in amplitude, the impurity rate first decreased and then increased, because the amplitude was too large or too small and the kernels and pods were beaten chaotically on the sieve surface; therefore, it was difficult to achieve effective stratification.

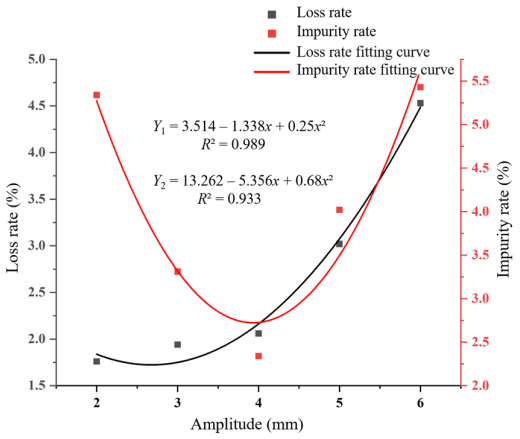


Figure 13. Effect of the amplitude on the cleaning performance.

4.3.3. Effect of Frequency on the Cleaning Performance

This section focuses on five different levels of frequency of the vibrating screen device, simulates the impact of these frequency levels (460 Hz, 480 Hz, 500 Hz, 520 Hz, and 540 Hz), and sets the fan speed to 1700 r/min and the amplitude to 4 mm, followed by the calculation of the kernel loss rate and impurity rate after the simulation.

As shown in Figure 14, with the gradual increase in vibration frequency, the kernel loss rate and the impurity rate slowly decreased and then rapidly increased. The reason is that with the increase in frequency, the vibrating screen transports the materials very quickly, resulting in the removal of kernels by the pods and, consequently, a high kernel loss rate. At the same time, when the frequency was too low, the extrudates could not be effectively separated, resulting in the discharge of the kernels and pods together and in an extremely high impurity content.

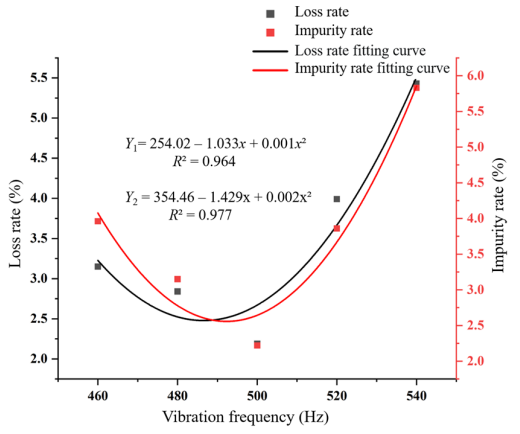


Figure 14. Effect of the vibration frequency on the cleaning performance.

4.4. Analysis of Simulation Results

4.4.1. Analysis of the Movement Law of Extrudates

As shown in Figure 15, the influencing factors are the distribution law of the airflow field and the state diagram of the particle states with different moments in the cleaning chamber, with the fan speed of 1700 r/min, the amplitude of 4 mm, and the vibration frequency of 480 Hz. The figure shows that at (t) = 0.5 s, the extrudate began to form, falling into the cleaning chamber from the inlet, followed by the rotation of fan blades and generation of airflow, which then passed through the bottom of the screen. At 1.5 s, under the combined action of the sieve surface vibration and the fan airflow, the pods and kernels began to separate and the airflow field in the cleaning chamber gradually stabilized. With the increase in time (t), the separation was evident at 3 s, and the intact kernels and half kernels moved toward the front side of the sieve, while the pods moved toward the back side of the sieve, and the airflow field in the cleaning chamber became stable. At 6 s, however, the cleaning process neared its completion, and most kernels were discharged from the kernels' outlet, while the pods were discharged towards the impurity outlet. At the time (t) = 10 s, the cleaning process finally ended.

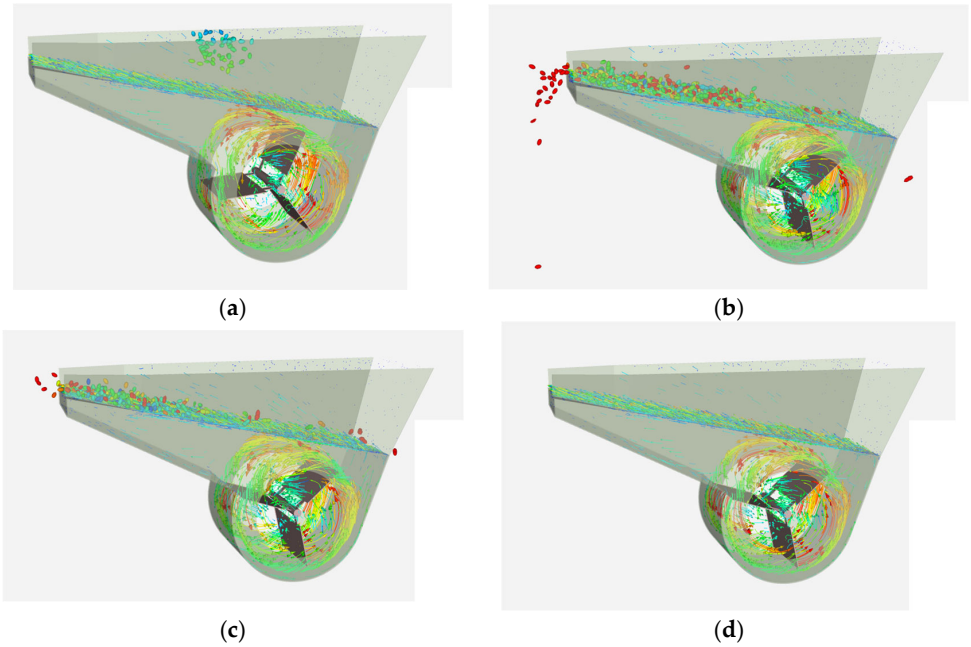


Figure 15. Diagram of transient simulation in the air–screen cleaning device. (**a**) The time is 0.5 s. (**b**) The time is 3 s. (**c**) The time is 6 s. (**d**) The time is 10 s.

Figure 16 demonstrates that the random extrudates in the air–screen cleaning fell under the influence of gravity and jumped after touching the sieve surface. Thereafter, under the combined action of airflow and vibration, the lighter peanut whole kernels (with a higher specific gravity) and the half kernels moved in a wave direction toward the mouth of the kernels, and the heavier peanut pods (with a lower specific gravity) were less affected by the induced airflow and moved toward the tail of the sieve after being thrown from a distance onto the sieve surface.

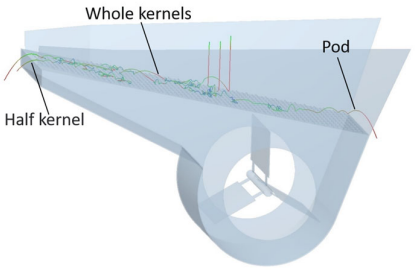
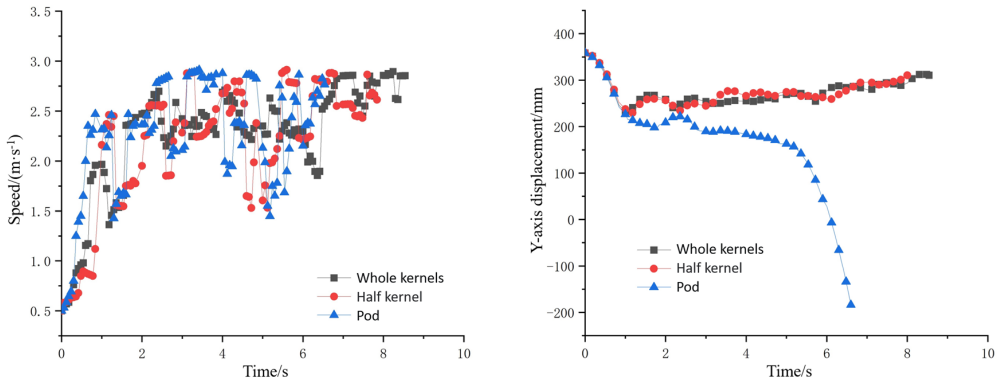


Figure 16. Trajectory of the extrudates.

4.4.2. Mechanism of the Motion Separation of Extrudates

The data on motion velocity and displacement of any single particle in the air–screen cleaning device were extrudates from the EDEM post-processing module and were then processed using the Origin 2021 software to obtain the movement speed and displacement time curve of particles.

As shown in Figure 17, the speed of the extrudates began to change greatly at 0.8 s, because the extrudates were affected by the vibration of the fish scale sieve surface and airflow, and the extrudates' movement during the course of the extrudates was manifested in a more complicated way. Furthermore, the speed fluctuation was evident, among which the difference between the maximum speed and minimum speed for intact kernels was 2.41 m/s, while this difference for half kernels was 2.25 m/s, and, for pods, it was 2.63 m/s. The change in displacement of the complete kernels along the y-axis in the air–screen cleaning device was 48.03 mm, whereas the axial displacement change in half kernels was 47.31 mm, and, for pods, it was 185.08 mm. After the extrudate in the air–screen cleaning device initially entered the airflow field, the displacement changes in the three above-mentioned materials in 0–1 s were similar and in 1–3 s, they still showed a similar pattern. These values indicate that these kernels were not completely stratified, and the pods were first discharged after 4 s, and then, the half kernels and intact kernels were released in turn after 6 s, reaching the farthest position.



(**a**) (**b**)

Figure 17. The curve representing the variation in the movement velocity and the y-axis displacement of particles in the air–screen cleaning device. (**a**) The particle velocity. (**b**) The y-axis displacement curve.

The above analysis of the speed, motion trajectory, and displacement changes in each extrudate shows that the separation of the extrudates was relatively smooth and thorough, and it occurred in a short time. This indicates that the values of the fan speed, amplitude, and frequency set for the simulation method were reasonable, and there were no problems, such as the lack of a regular contact of the extrudates on the sieve surface, as well as a poor and incomplete separation.

4.5. Orthogonal Simulation Test and Analysis of Results

4.5.1. Orthogonal Experimental Design

To obtain the best working parameters of the air–screen cleaning device, according to the results of the single-factor simulation test, the three factors, including the fan speed (X_1), amplitude (X_2), and vibration frequency (X_3), were selected as the independent variables, and the kernel loss rate and impurity rate were used as indicators. Moreover, the Design–Expert 12.0 software was used to carry out orthogonal experimental tests based on the single-factor optimization method results [32,33]. The experimental factors and their levels are shown in Table 6.

Table 6. Levels of experimental factors.

Level	Experimental Factors		
	Fan Speed X_1/(r min^{-1})	Amplitude X_2/mm	Vibration Frequency X_3/Hz
−1	1600	3	480
0	1700	4	500
1	1800	5	520

To obtain the optimal parameter combination, the three-factor and three-level response surface analysis method was designed according to the Box–Behnken experimental design principle, including a total of 17 sets of tests. The test protocol and results are shown in Table 7.

Table 7. Experimental design and results.

Serial Number	Factor			Loss Rate Y_1/%	Impurity Rate Y_2/%
	X_1	X_2	X_3		
1	0	1	1	4.97	4.75
2	0	0	0	2.39	1.79
3	1	−1	0	3.03	3.76
4	0	0	0	2.12	2.03
5	−1	0	1	4.56	4.64
6	−1	1	0	4.47	3.84
7	0	−1	1	3.39	4.66
8	0	0	0	2.43	1.98
9	0	1	−1	4.34	3.75
10	0	0	0	2.03	2.00
11	1	1	0	5.02	4.93
12	0	−1	−1	1.91	3.11
13	1	0	1	3.69	4.57
14	1	0	−1	3.66	4.18
15	−1	−1	0	1.75	4.07
16	0	0	0	2.06	2.02
17	−1	0	−1	2.00	3.17

4.5.2. Regression Models and a Test of Significance

According to the orthogonal experimental data provided in Table 7, the Design–Expert 12.0 software was used to perform quadratic polynomial regression analysis [34–36], and the response surface method was used to analyze and study the law of influence of the correlation between and the interaction effect of each factor. The quadratic polynomial regression models of the kernel loss rate (Y_1) and the impurity rate (Y_2) were established involving the factors of fan speed X_1, vibration frequency X_2, and amplitude X_3, as follows:

$$Y_1 = 2.21 + 0.3275X_1 + 1.09X_2 + 0.5878X_3 - 0.6325X_1X_3 + 0.5932X_1^2 + 0.7682X_2^2 + 0.6783X_3^2 \quad (11)$$

$$Y_2 = 1.96 + 0.215X_1 + 0.2087X_2 + 0.5513X_3 - 0.35X_1X_2 - 0.27X_1X_3 + 1.13X_1^2 + 1.06X_2^2 + 1.05X_3^2 \quad (12)$$

The analysis of variance (ANOVA) using the regression model showed that the significance level (p) of the regression models for the kernel loss rate Y_1 and the impurity rate Y_2 was less than 0.01, indicating the highly significant influence of these two models. The significance level (p) of the model misfit was greater than 0.05, and the imitation was not significant. The coefficient of determination (R^2) of the models was greater than 0.98 (0.9832 and 0.9948, respectively), indicating that the two models could explain more than 98% of the evaluation indices, and, therefore, they can be used for parameter optimization. According to the regression coefficients of each factor in these two models, each factor in relation to the working parameters of the air–screen cleaning device was found to have a significant influence on the kernel loss rate, and the order of the degree of influence was amplitude > vibration frequency > fan speed. The influence of each factor on the impurity rate was significant, and the order of the degree of influence was vibration frequency > fan speed > amplitude, which was consistent with the results obtained from the single-factor simulation test, indicating that the CFD–DEM method was reliable.

4.5.3. The Effect of the Interaction Factors on Kernel Loss Rates

Figure 18 shows the response of the interaction factor to the kernel loss rate Y_1 based on the response surface method.

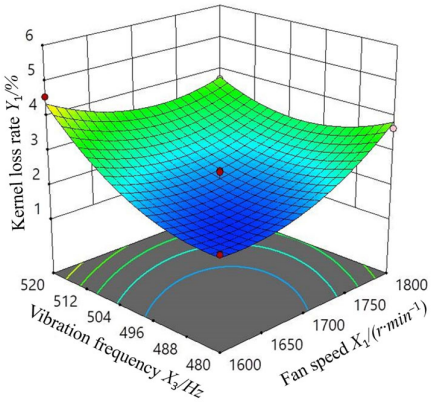
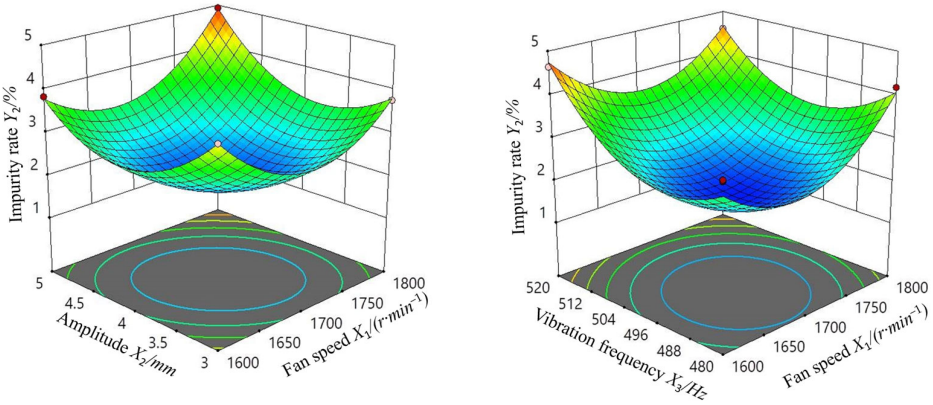


Figure 18. Effect of the machine's fan speed and vibration frequency on kernel loss rate.

When the amplitude was at the zero level, with the increase in fan speed and vibration frequency, the kernel loss rate showed a slow downward trend, and the change in the fan speed and vibration frequency had obvious effects on the response. Furthermore, the interaction between these factors had a significant impact on the kernel loss rate because the fan speed changes affected the airflow within the cleaning chamber, which consequently affected the movement of the extrudates. The regression equation for the kernel loss rate was obtained as follows: fan speed, 1693.7 r/min; amplitude, 3.29 mm; and vibration frequency, 497.75 Hz, corresponding to a kernel loss rate of 1.65%.

4.5.4. The Effect of the Interaction Factors on Impurity Rate

Figure 19 shows the response of the interaction factor to the impurity rate (Y_2). Figure 19a demonstrates the response surface diagram of the interaction between amplitude and fan speed on the impurity rate when the vibration frequency is 0. The amplitude and fan speed showed a trend of decreasing first and then increasing in relation to the impurity rate, and the interaction had a highly significant influence on the impurity rate.



(**a**) (**b**)

Figure 19. Effects of the interaction of factors on the impurity rate. (**a**) Effect of the machine's fan speed and amplitude on the impurity rate. (**b**) Effect of the machine's fan speed and vibration frequency on the impurity rate.

Figure 19b shows that with the increase in fan speed and vibration frequency, the impurity rate decreased slightly and then rose rapidly. The rising trend of vibrating frequency was obvious, and the influence of the vibrating frequency on the impurity rate was slightly greater than that of the fan speed, with their interaction having a greater and highly significant impact on the impurity rate. The extreme value miscellaneous regression equation was developed, and the best parameter combination obtained is as follows: a fan speed of 1688.6 r/min, amplitude of 3.9 mm, and vibration frequency of 494.3 Hz, corresponding to a 1.86% impurity rate.

4.6. Parameter Optimization

To further improve the cleaning performance of the cleaning device, combined with the test results and ANOVA, a full-factorial quadratic regression model for performance indicators was established to optimize the target and find the optimal parameters [37,38]. Based on the principle of the kernel loss rate Y_1 and the lowest impurity rate Y_2, a mathematical model was established as follows:

$$\begin{cases} minY_1(X_1, X_2, X_3) \\ minY_2(X_1, X_2, X_3) \\ \\ s.t. \begin{cases} -1 \le X_1 \le 1 \\ -1 \le X_2 \le 1 \\ -1 \le X_3 \le 1 \end{cases} \end{cases} \quad (13)$$

Based on a pair of the optimization module solutions (13) in the Design–Expert 12.0 software, according to the kernel loss rate and the impurity rate of 1:1, the optimal parameter combination obtained is as follows: a fan speed of 1682.72 r/min, an amplitude of 3.74 mm, and a vibration frequency of 492.86 Hz, corresponding to a kernel loss rate of 1.75% and an impurity rate of 1.89%.

4.7. Validation Experiments

The improved air–screen cleaning device was applied to the peanut sheller to carry out the cleaning test of the peanut sheller (Figure 20). The test materials and methods are provided in Section 2.



Figure 20. Cleaning test.

Since the actual working parameters were difficult to adjust to the optimized value of the theoretical solution, a set of parameters with values close to the optimized value were selected for experimental verification. The parameter values were a fan speed of 1680 r/min, amplitude of 3.7 mm, and vibration frequency of 490 Hz.

As shown in Table 8, with the combination of the defined parameters at these values, the average kernel loss rate and impurity rate were found to be 2.01% and 2.42%, respectively, and those values obtained after the improvement and optimization were reduced by 3.71 and 4.42 percentage points compared with the pre-optimized values (original values), respectively, indicating a significant improvement of the cleaning performance.

Table 8. Experimental results of the optimal parameters test.

Serial Number	Loss Rate (%)	Impurity Rate (%)
1	2.14	2.45
2	1.97	2.29
3	2.10	2.41
4	1.89	2.57
5	1.95	2.38
Average value	2.01	2.42
Original value	5.72	6.84
The industry standard values	≤3	≤3

5. Conclusions

This paper aimed to model the cleaning device and hulling extrudates of the HT–1000 peanut sheller. The main structural parameters and working parameters of the CFD, DEM, and CFD–DEM coupling methods were used to optimize its main structural parameters and working parameters, and the optimal parameter combination was obtained, effectively improving the machine's cleaning performance.

(1) Under the working conditions of a fan speed of 1900 r/min, amplitude of 3 mm, and vibration frequency of 520 Hz, the processes of peanut hulling and cleaning were carried out, and the disadvantages of the air–screen cleaning device were found. Through the force analysis of the extrudates, the key parameters that could affect its cleaning performance were obtained.

(2) The improved scheme of optimizing the installation angle of the screen surface of the air–screen cleaning device was proposed, and through a simulation and comparative

analysis before and after the structural improvement of the device, the uniformity of the fluid flow in the cleaning chamber was improved after the adjustment of the screen surface angle so that a more reasonable airflow distribution could be achieved.

(3) The CFD–DEM coupling simulation technology was used to explore the movement trajectory, velocity, and displacement of each component of peanut extrudates in the cleaning chamber. In addition, the separation law of extrudates was characterized, and the parameter ranges for each factor were determined via a single-factor simulation experiment.

(4) Based on the central composite Box–Behnken design, an orthogonal simulation optimization for the air–screen cleaning device was carried out, and the obtained optimal parameter combination is as follows: a fan speed of 1682.72 r/min, amplitude of 3.74 mm, and vibration frequency of 492.86 Hz.

(5) Through the hulling and cleaning processes in the machine, the accuracy of the simulation results was verified. Using parameters of a fan speed of 1680 r/min, an amplitude of 3.7 mm and a vibration frequency of 490 Hz, the kernel loss rate and the impurity rate were 2.01% and 2.42%, 3.71 and 4.42 percentage points lower than those before optimization, respectively, which indicated that the cleaning performance of the device was significantly improved.

Author Contributions: Conceptualization, writing—original draft, Y.Y.; methodology, Y.Y. and Z.L.; Software, formal analysis, Y.Y., Z.L. and J.W.; investigation, validation, Z.K. and F.H.; writing—review and editing, Y.Y., Z.L., J.W., F.H. and Z.K.; funding acquisition, L.G. and Z.L. All authors have read and agreed to the published version of the manuscript.

Funding: This research was funded by the National Key Research and Development Project Plan of China (Program No. 2016YFD0702102), and the National Natural Science Foundation of China (Program No. 51575367), and the Department of Education Project of Liaoning Province (Program No. LJKMZ20220997), and Graduate Innovation Cultivation Funding Project of Shenyang Agricultural University (Program No. 2022YCZS02).

Institutional Review Board Statement: Not applicable.

Informed Consent Statement: Not applicable.

Data Availability Statement: Not applicable.

Conflicts of Interest: This research received no external funding.

References

1. Lu, R.; Gao, L.; Chen, C.; Butts, C.L. Characteristics of peanut hulling and processing technology in the United States and inspiration. *Trans. Chin. Soc. Agric. Eng.* **2019**, *35*, 287–298.
2. Li, H.; Wang, Q.; Li, J.; Zhang, Y. Design and experiment of destoned cleaning device of half–fed peanut combine harvester. *J. Chin. Agric. Mech.* **2021**, *42*, 29–33.
3. Liu, D.; Sun, Q.; Liu, L.; Qian, K.; Jin, T.; Wang, D.; Li, X. Simulation analysis and test of air–suction peanut shell kernel cleaning device. *J. Jiangsu Agric. Sci.* **2022**, *50*, 162–167.
4. Li, X.; Sun, Q.; Liu, L.; Liu, D.; Xu, W.; Qian, K.; Chen, K.; Wang, D.; Zhang, C. Design and test of strip–slit peanut kernel grading test bench. *J. Shenyang Agric. Univ.* **2022**, *53*, 701–708.
5. Lu, R.; Gao, L.; Liu, Z.; Yang, D. Development status and prospect of peanut sheller technology in China. *J. Shenyang Agric. Univ.* **2020**, *51*, 124–133.
6. Lu, R.; Liu, Z.; Gao, L.; Yang, D. Development of air suction and cleaning device for peanut sheller in vertical conical community. *Trans. Chin. Soc. Agric. Eng.* **2020**, *36*, 23–30.
7. Wang, J.; Liu, J.; Hu, Z.; Xie, H.; Peng, B.; Yan, J.; Chen, Y. Optimization of key operating parameters of peanut seed belt cleaning equipment. *Trans. Chin. Soc. Agric. Eng.* **2018**, *34*, 33–41.
8. Gao, L.; Hui, Z.; Dong, H.; Xu, Z.; Liu, Z.; Li, H. Design and experiment of peanut sheller for three–roller community breeding. *Trans. Chin. Soc. Agric. Mach.* **2016**, *47*, 159–165.
9. Liu, C.; Wang, S.; Shi, Q.; Geng, L.; Yang, F. Design of test bench of peanut combine harvester cleaning system. *J. Agric. Mech. Res.* **2018**, *40*, 91–95.
10. Guo, Z.; Qiu, Y.; Yan, X.; Wang, J.; Si, S.; Guo, F.; Zhang, F. Research on the Resistance Reduction Law of Self-Excited a Resonant Circular Arc-Surface Bulldozing Plate Based on the Discrete Element Method. *Agriculture* **2023**, *13*, 1880. [CrossRef]

11. Shi, Y.; Xiang, S.; Xu, M.; Huang, D.; Liu, J.; Zhang, X.; Jiang, P. Design and Experimental Study of Ball-Head Cone-Tail Injection Mixer Based on Computational Fluid Dynamics. *Agriculture* **2023**, *13*, 1377. [CrossRef]
12. El-Emam, M.A.; Zhou, L.; Omara, A.I. Predicting the performance of aero-type cyclone separators with different spiral inlets under macroscopic bio-granular flow using CFD–DEM modelling. *Bio. Eng.* **2023**, *233*, 125–150. [CrossRef]
13. Zhang, Z.; Shi, G.; Li, J.; Wang, X.; Ding, L.; Wang, L. Analysis of jujube movement characteristics under positive and negative pressure airflow based on CFD-DEM. *Comput. Electron. Agric.* **2023**, *210*, 107902.
14. Hou, J.; Liu, X.; Zhu, H.; Ma, Z.; Tang, Z.; Yu, Y.; Jin, J.; Wang, W. Design and Motion Process of Air-Sieve Castor Cleaning Device Based on Discrete Element Method. *Agriculture* **2023**, *13*, 1130. [CrossRef]
15. Chen, X.; Hu, G.; Zhao, T.; Li, Z.; Zhou, J. Simulation study on negative pressure winnowing of walnut shell kernel mixture based on CFD–DEM coupling. *J. Shandong Agric. Univ.* **2021**, *52*, 1017–1027.
16. Mu, G.; Lv, H.; Zhang, T.; Zheng, W.; Zhang, W.; Lv, Z. Gas–solid interaction simulation and experimental optimization of throwing device of sweet potato straw recycling machine. *Trans. Chin. Soc. Agric. Mach.* **2021**, *52*, 213–222.
17. Shi, R.; Dai, F.; Zhao, W.; Liu, X.; Wang, T.; Zhao, Y. Simulation optimization and experiment of compound cleaning system of hilly and mountainous flax combine harvester. *Trans. Chin. Soc. Agric. Mach.* **2022**, *53*, 93–102.
18. *GB/T 2828.1-2012*; Count Sampling Detection Procedure. China Standards Press: Beijing, China. Available online: https://www.doc88.com/p-7985024596928.html/ (accessed on 8 September 2022).
19. *GB/T 5262-2008*; General Provisions for Methods for Determining Test Conditions for Agricultural Machinery. China Standards Press: Beijing, China. Available online: https://www.doc88.com/p-8532978484570.html/ (accessed on 7 September 2022).
20. *GB/T 5983-2013*; Cleaning Machine Test Method. China Standards Press: Beijing, China. Available online: https://www.jianceye.com/biaozhun/gb-t-5983-2013/ (accessed on 8 September 2022).
21. *GB/T 5982-2017*; Thresher Test Method. China Standards Press: Beijing, China. Available online: https://www.doc88.com/p-0963884986579.html (accessed on 7 September 2022).
22. Li, H.; Li, Y.; Tang, Z.; Xu, L. Numerical simulation of CFD–DEM of material motion on vibrating screen of air screen cleaning device. *Trans. Chin. Soc. Agric. Mach.* **2012**, *43*, 79–84.
23. Tong, S.; Shen, Q.; Tang, N. Numerical simulation and optimization test of mixed flow field of longitudinal axial flow cleaning device. *Trans. Chin. Soc. Agric. Mach.* **2016**, *47*, 135–142.
24. Wang, J.; Gao, L.; Liu, Z.; Yang, D. Peanut pods mechanical properties research. *J. Agric. Mech. Res.* **2017**, *39*, 182–186.
25. Gao, L.; Zhang, W.; Du, X.; Liu, X.; Yang, J.; Liu, M. Experiment on floating coefficient of outfall from peanut sheller. *Trans. Chin. Soc. Agric. Mach.* **2012**, *28*, 289–292.
26. Gong, F.; Hu, M.; Bao, A.; LI, D.; Gao, T.; Wang, C. Parameter calibration and significance analysis of straw based on Hertz–Mindlin model. *J. Xinan Univ.* **2022**, *44*, 186–196.
27. Lei, X.; Wu, W.; Deng, X.; Li, T.; Liu, H.; Guo, J.; Li, J.; Zhu, P.; Yang, K. Determination of Material and Interaction Properties of Granular Fertilizer Particles Using DEM Simulation and Bench Testing. *Agriculture* **2023**, *13*, 1704. [CrossRef]
28. Qian, Z.; Jin, C.; Yuan, W.; Ni, Y.; Zhang, G. Frictional impact dynamics model of threshing process between flexible teeth and grains. *J. Jilin Univ.* **2021**, *51*, 1121–1130.
29. Wang, B.; Yu, Z.; Hu, Z.; Cao, M.; Zhang, P.; Wang, B. Numerical simulation and experiment of flow field of peanut picking and harvesting machine three–wind system winnowing system. *Trans. Chin. Soc. Agric. Mach.* **2021**, *52*, 103–114.
30. Liao, Q.; Yang, B.; Li, X.; Liao, Y.; Zhang, N. Simulation and test of air chamber flow field of internally inflated blown–type rapeseed precision seeder. *Trans. Chin. Soc. Agric. Mach.* **2012**, *43*, 51–54.
31. Liu, H.; Gong, Y.; Zhang, B.; Chen, Y.; Zhou, M. Design and optimization of working parameters of fry sorter based on EDEM. *Trans. Chin. Soc. Agric. Mach.* **2020**, *51*, 114–121.
32. Yang, M.; Zhang, Y.; Zhang, C.; Gu, F.; Yu, Z.; Hu, Z. Design and experiment of peanut membrane rice separation device combined by kneading and then separating air screen. *Trans. Chin. Soc. Agric. Mach.* **2020**, *51*, 112–121.
33. Lu, R.; Yang, D.; Gao, L.; Liu, Z.; Liu, M.; Shen, Y. Design and experiment of vertical cone Drum Type Peanut sheller. *Trans. Chin. Soc. Agric. Mach.* **2019**, *50*, 114–123.
34. Mao, S.; Zhou, J.; Chen, Y. *Experimental Design*, 2nd ed.; China Statistics Press: Beijing, China, 2012.
35. Wang, L.; Feng, X.; Wu, Z. Design and test of stepwise vibrating screen for corn combine harvester. *Trans. Chin. Soc. Agric. Mach.* **2018**, *49*, 115–123.
36. Shi, L.; Hu, Z.; Gu, F. Design and parameter optimization of peanut residual film recycling machine for rake ridge cropping. *Trans. Chin. Soc. Agric. Eng.* **2017**, *33*, 8–15.
37. Zhang, X.; Liu, J.; Shi, Z. Design and parameter optimization of reverse membrane–soil separation device of residual membrane recovery machine. *Trans. Chin. Soc. Agric. Eng.* **2019**, *35*, 46–55.
38. Wang, L.; Ma, Y.; Feng, X.; Song, L.; Chai, J. Design and experiment of sectional vibrating screen cleaning device for maize grain harvester. *Trans. Chin. Soc. Agric. Mach.* **2020**, *51*, 89–100.

Disclaimer/Publisher's Note: The statements, opinions and data contained in all publications are solely those of the individual author(s) and contributor(s) and not of MDPI and/or the editor(s). MDPI and/or the editor(s) disclaim responsibility for any injury to people or property resulting from any ideas, methods, instructions or products referred to in the content.